Zn-Al Layered Double Hydroxide Film Functionalized by a Luminescent Octahedral Molybdenum Cluster: Ultraviolet-Visible Photoconductivity Response

Thi Kim Ngan Nguyen, Noee Dumait, Fabien Grasset, Stéphane Cordier, David Berthebaud, Yoshio Matsui, Naoki Ohashi, Tetsuo Uchikoshi

Zn-Al Layered Double Hydroxide Film Functionalized by Luminescent Octahedral Molybdenum Cluster: Ultraviolet-Visible Photoconductivity Response

Thi Kim Ngan Nguyen[a,b,*], Noée Dumait[c], Fabien Grasset[a,b,c], Stéphane Cordier[c], David Berthebaud[b], Yoshio Matsui[a], Naoki Ohashi[a,b], Tetsuo Uchikoshi[a,b,*]

[a]Research Center for Functional Materials, National Institute for Materials Science (NIMS), 1-2-1 Sengen, Tsukuba, Ibaraki 305-0047, Japan

[b]CNRS–Saint-Gobain–NIMS, UMI 3629, Laboratory for Innovative Key Materials and Structures (LINK), National Institute for Materials Science, 1-1 Namiki, Tsukuba, Ibaraki 305-0044, Japan

[c]Univ. Rennes-CNRS-Institut des Sciences Chimiques de Rennes, UMR 6226, 35000 Rennes, France

KEYWORDS: molybdenum cluster, layered double hydroxide, photoconductivity, photoluminescence, photodetector

ABSTRACT

A novel UV-Vis photodetector consisting of an octahedral molybdenum cluster-

functionalized Zn_2Al layered double hydroxide (LDH) has been successfully synthesized by co-precipitation and delamination methods under ambient conditions. The electrophoretic deposition process has been used as a low cost, fast, and effective method to fabricate thin and transparent nanocomposite films containing a dense and regular layered structure. The study provided evidence that the presence of the Mo_6 cluster units between the LDH does not affect the ionic conduction mechanism of the LDH, which linearly depends on the relative humidity and temperature. Moreover, the photocurrent response is remarkably extended to the visible domain. The reproducibility and stabilization of the photocurrent response caused by the Mo_6 cluster-functionalized LDH have been verified upon light excitation at 540 nm. Additionally, it was demonstrated that the films show advantageously strong adherence properties for application requirements.

1. INTRODUCTION

Energy converters based on nanoarchitecture-cluster functionalized materials with stabilization of the physicochemical properties have been developed for materializing a sustainable society. Particularly, the efficiency and applicability of the light energy converters or photodetectors essentially depend on their light sensitivity performance, fast photocurrent response speed, and a linear dependence of the optical and current values in

the industry. During the last few decades, the use of various wide band-gap semiconducting inorganic materials, such as ZnO, MoS_2, ZnS, SiC for the light energy converters, has been mainly reported due to their simple structure and high photoconductive gain.[1-4] The visible (Vis) sensing photodetector using solar light energy became an interesting study for sustainable energy development goals.[5, 6] However, the development of broadband photodetectors, having an efficient photoactivity in the UV-Vis light range, low cost, and environmentally friendly material and process, is facing many challenges for researchers. The layered double hydroxide (LDH), one of the promising inorganic matrices for the nanocomposite, was expressed by the formulation of $[M^{2+}_{1-x}M^{3+}_{x}(OH)_2]^{x+}$ $(A^{n-})_{x/n}\cdot mH_2O$ (M^{II} = Zn, Ni, Co, Mn, etc.; M^{III} = Al, Fe, etc.; A = NO_3^-, CO_3^{2-}, SO_4^{2-}, PO_4^{3-}, etc.) with x as the molar ratio $M^{2+}/(M^{2+} + M^{3+})$ in the range of 0.2–0.33 and A^{n-} as an n-valent anion. LDH is well known as a multifunctional material with easily scalable fabrication and flexible application for a catalyst,[7] water treatment,[8] and drug support.[9] The tunability of the trivalent atom metal in an edge-sharing $M(OH)_6$ octahedral network and internal anion exchangeability increase the chance to fabricate a wide variety of different LDH-based materials in a large amount. This is mostly due to the distinction of tunable host layers and functional interlayer guest molecules.[10] Currently, several studies been comprehensively focused on adsorbability improvement,[11,

[12] or hydroxyl anionic conductivity[13-16] of the LDH, following the modification of the elemental compositions and charge densities of the host layers. As a result, the LDH-based applications have focused on the device's performances as humidity sensors,[17] gas sensors,[18,19] optical pH sensors,[20] and super-capacitor.[21-23] Particularly, the LDH or photo-functional LDH-based materials have shown promising features for applications in optical devices. For example, G. Prestopino et al. reported the switchable photoluminescent properties of dehydrated Zn/Al-LDH nano-platelets through a dehydration–hydration process.[24] The luminescent organic molecule or quantum dot modified LDH has also been remarkably studied for use in photochemical cells.[25-27]

Recent studies have highlighted the LDH-based materials as potential candidates for photodetector applications due to their photocurrent response under UV-Vis light. For instance, the ZnAl LDH nanosheet scrolls present a photoresponse in the UV spectral range below 420 nm, indicating a visible-blind spectral response.[28] Extending the photocurrent response in the visible range was performed by adding the TiO_2 component to the ZnFeAl-layered double hydroxides, involving a better photocathodic protection performance for 304SS stainless steel due to the unique structure and efficient visible-light response property.[29] In addition, the photo-induced charge combination in the ultrathin-layered double hydroxide nanosheets under light illumination could accelerate

the oxygen evolution reaction.[30] Finally, the studies of the photodetector made from the LDH-based materials have motivated researchers to optimize their stable photochemical properties for industrial applications.

In this study, a new potential photodetector material exhibiting a UV–Vis photoconductivity response was fabricated from Zn_2Al LDH intercalated glycine (abbreviated as ZAG) functionalized by octahedral iodide-bridged molybdenum clusters (abbreviated as Mo_6). This octahedral metal cluster (MC) is illustrated by an organic-inorganic building unit with a 1.2-nm size and belongs to the family composed of the $\{M_6L^i_8\}^{4+}$ (M = Mo, W, Re; L^i = inner halide ligand) metallic cores bonded with 6 apical ligands (L^a = Cl, Br, I or $OCOC_nF_{2n+1}$…).[31,32] The Mo_6 MCs have been known for several decades for their luminescence[33-36] and redox properties.[37,38] The photochemical and electrochemical properties of the MC come from the metal-metal and metal-ligand bonding, resulting in a strong absorption in both the UV-Vis lights and a prominent luminescent emission within the deep red/near-infrared (NIR) regions. The remarkable optical properties of the Mo_6 MC are their i) high quantum yield, ii) large Stoke shift that avoids re-absorption losses, iii) strong luminescence, iv) phosphorescence in the infrared range, and v) UV-Vis absorption combined with an excellent photostability due to its

unique complex structure. The applicable potentials of these MCs have been proved through the recent developments of the optical-related inorganic devices, such as photocatalytic water purification,[39] nanoparticles for bioimaging,[40] photoelectrodes for solar cells[41] and photonic crystals.[34] The flexible interactions between the metal cluster core, apical ligand, and counter ion in the nanocomposite have become a challenge to figure out the right explanation for the optical property modification. However, it also provides a new approach to develop a new molybdenum cluster-based device with a controlled optical property based on the modification of the elemental compositions and their physicochemical interactions.

The electrophoretic deposition (EPD) process, a thin film coating technique which is able to easily control the homogeneity, thickness, compatibility, and maximum loading ability of the main functional compositions, possibly allows the applicability of the cluster bulk materials. Considering the advantages of the EPD process, it will be a smart technique to fabricate thin films on the devices, particularly, for the devices based on the MCs. Very recently, this method was successfully used to fabricate thin and transparent pure clusters or hybrid nanocomposite films with very interesting properties for energy-saving

applications.[42]

A Mo_6 cluster compound, namely $Cs_2[Mo_6I^i_8I^a_6]$ (abbreviated as CMI), with strong absorption in the visible light up to 600 nm has been selected for its photoresponse under broad visible light. Meanwhile, Zn-Al LDH (ZA) gives a photoresponse when excited by ultraviolet (UV) light. A thin and transparent Mo_6-functionalized LDH film (~ 3µm) was successfully prepared by the EPD process, exhibiting a dense lamellar structure. The Mo_6-functionalized LDH film exhibited several interesting complementary properties, i.e., i) a red emission centered at the wavelength of 690 nm by UV-Vis light irradiation, ii) an anionic conductivity of about 10^{-6} $S.cm^{-1}$ with an activation energy (E^a) of about 1.08 eV, iii) a proper photocurrent response under UV-Vis light excitation ranging from 320 to 540 nm, and iv) a photocurrent response depending on the film thickness, temperature, and humidity. The remarkable point in this study is the determining of the relation between the photoresponse and the temperature or the humidity level which has not been figured out, to the best of our knowledge, in previous reports about LDH-based materials.[28-30] Even if a further understanding of this phenomenon should be investigated in the future, we have demonstrated that EPD is an excellent process to easily prepare a Mo_6-functionalized LDH film exhibiting good mechanical properties.

2. EXPERIMENTAL SECTION

2.1 Chemicals

$Zn(NO_3)_2 \bullet 6H_2O$ (99%) and $Al(NO_3)_3 \bullet 9H_2O$ (98%, pH= 2~4) were purchased from Chameleon reagent. Glycine (99%) was purchased from the Fujifilm Wako Pure Chemical Collaboration. The sodium hydroxide (NaOH, 5 mol/L), acetone (99.5%) and formamide (98.5%), and methyl ethyl ketone (MEK, 99%) were supplied from Nacalai Tesque. All chemicals were used without purification. The deionized water was obtained from Water Purifiers WG710 equipment with the conductance of 0.5×10^{-4} S/m at 25°C.

2.2 Synthesis of CMI, LDH-Zn_2Al (ZA) and glycine-modified LDH-Zn_2Al (ZAG)

The CMI cluster powder was synthesized following the procedure reported in a previous publication,[43] i.e., by the reaction of CsI (Alfa Aesar 99.9 %) and MoI_2 at the temperature of 700°C. The Zn_2Al LDH powder, abbreviated ZA, was synthesized by the co-precipitation method in air with the ratio between the Zn and Al atoms (Zn/Al = 2) referenced from the report of Ahmed et al.[44] In greater detail, a transparent mixed solution of $Zn(NO_3)_2 \bullet 6H_2O$ (0.02 mol) and $Al(NO_3)_3 \bullet 9H_2O$ (0.01 mol) was prepared in 50 mL of deionized water using a magnetic stirrer for 1 h. The solution was then titrated by NaOH (5 M) at the pH value of 10 to obtain a cloudy suspension, then agitated at room

temperature for 24 h to increase the crystallinity of the LDH. This powder was washed and dried at 80ºC for more than 24 h and used as the reference material.

A glycine-modified Zn_2Al LDH, abbreviated ZAG, was similarly synthesized following the ZA-synthesized steps with the simultaneous dissolution of the glycine (0.01 mol) in an aqueous salt solution. ZAG was purified by washing in deionized water until the pH was between 7 and 8, then dried at 60ºC for 24 h. The ZAG nanosheets were then obtained by a delamination process in formamide for subsequently functionalizing the CMI cluster. Glycine and formamide were chosen as the amino acid anion intercalant and polar solvent systems, respectively, for the exfoliation process as first described by Hibino and Jones.[45]

2.2 Synthesis of the CMI Cluster@ZAG Powders and Films

The CMI powder was first dissolved in formamide at the concentration of 0.4 g/L using an ultrasonic water bath for 1 h to obtain a red homogeneous solution. The glycine was added to this red CMI solution, then agitated by a magnetic stirrer for 2 days. Table S1 displays the compositions and ratios between the glycine and the Mo_6 cluster abbreviated CGx with x=1, 2, 3, 4 as an abbreviated representation of the real weight. Secondly, the as-synthesized ZAG powder with 10 times the weight of the CMI cluster was added to the CGx suspensions, then continually agitated for 3 days. The washing procedure of the

CGx@ZAG wet powders in formamide was repeated three times to eliminate the residual cluster and glycine and stored at room temperature for the film fabrications. Only the CG1@ZAG wet powder was completely dried at 80ºC for X-ray diffraction (XRD), high-resolution transmission electron microscopy (HR-TEM), and optical characterizations for reference. In parallel, the ZAG powder was also dissolved in formamide at the concentration of 4 g/ L for 3 days without the CG mixture for preparing the delaminated wet ZAG powder.

The EPD system was built by two indium tin oxide-coated glass (ITO glass) slides with a surface area of 1.0×2.5 cm^2, acting as the anodic or cathodic electrodes (Geomatec Co., Ltd., Tokyo, Japan; 6.15-7.27 Ohm/sq), and was connected to a Source Meter (Keithley Model 2400, Ohio, USA) as an electric field generator. The schematic illustration of the nanocomposite film preparation by EPD is illustrated in Figure S1. The EPD suspensions were composed of the ZAG or CGx@ZAG wet powder dissolved in MEK (~ 2.5 g/L) using an ultrasonication treatment for 30 minutes. A small amount of formamide (~ 1 ml) was added to the suspension to increase the solubility of the CGx@ZAG in MEK and the stabilization of the suspension during the EPD process. With a positive zeta potential value as noted in Table S2, the cathodic EPD process was applied for the ZAG or CGx@ZAG film fabrication. During the EPD process, the applied voltage controls the

migrating speed of the charged particles to the electrodes as well as the homogeneity of the deposited particle size inside the film. Meanwhile, the deposition time directly impacts the formation of an insulator film that limits the force of the electric field on the ionic movement in the slurry. The film fabrication was operated at 15 V for 2 minutes or 25 V for 3 minutes to obtain the best properties.

2.3 Measurement of the Impedance and Current of the Films under Illumination, Temperature and Humidity Conditions

A schematic diagram of the impedance measuring system is illustrated in Figure S2. The ZAG or CGx@ZAG films deposited on the ITO-coated glass were contacted with a blank ITO-coated glass as the counter electrode with the measured area of 1 cm^2. The two electrodes were connected by a micrometer. The film thickness was estimated to be 3 to 4 μm by measurement using a 3D color microscope. The experimental conditions were controlled by a bench-top type temperature and humidity chamber (SH-222, Espec Corp.). The different UV-Vis light illuminations were generated by a 300 W compact Xenon light source (MAX-303, Asahi Spectra Co., Ltd.). A monochromator combined with an optical filter (Transmittance ~ 80 %) was used to generate monochromatic light with peaks centered at 320, 350, 370, 410, 440, 540, and 580 nm followed by the bandwidth of the light of about 10 nm. The electrical impedance of the films was measured by a 1260A

impedance analyzer (Solartron analytical, AMETEK Scientific Instruments) at the applied voltage of 500 mV in the frequency range between 10^1 Hz and 10^7 Hz. A source meter (Keithley Model 2400, Ohio, USA) was used to measure the photocurrent response of the films at a bias of 1 V in the controlled environmental conditions. The ZAG and CGx@ZAG films were prepared at 25 V as an upper limit of the applied voltage in order to obtain the optimal thickness with a relative dense and transparency for 2 minutes. The thickness is directly proportional to the amount of the adsorbed water as an important carrier whereas the high condense layered structure distributes to the moving pathway of the ions inside the material. The electrical conductivity was expressed by the following equation:

$$\sigma = l/(R.A) \quad (1)$$

where σ is the electrical conductivity, l is the thickness of the film, A is the area of the sample (1×1 cm^2), and R is the total resistance measured by Electrochemical Impedance Spectroscopy (EIS).

2.4 Characterization

The zeta potentials of the suspensions were determined by a zeta-potential analyzer (Zetasizer Nano Z, Malvern Instrument, Ltd., UK). The average hydrodynamic diameters and distribution of the LDH nanosheets in a MEK/ formamide medium were measured

by an ultrafine particle analyzer (Nanotrac NPA151 - Nanotrac ULTRA, Microtrac, Inc., USA) incorporated with the controlled reference method (CRM) in a dynamic light scattering (DLS) instrument. The crystalline layered structure of the powders and films were determined by XRD (SmartLab, RIGAKU, 40 kV and 30 mA) in the 2θ angle range from 1° to 50° at the scan speed of 1°/min with Cu Kα radiation (λ = 1.54 Å). The surface morphology and elemental composition were analyzed by field emission scanning electron microscopy (FE-SEM, S4800, Hitachi High-Technologies Corp.) at 5 kV coupled with an energy-dispersive X-ray (EDX) analysis device. High-resolution observations of the powder and films were performed by HR-TEM (JEOL JEM 2100F) equipped with an EDX analysis device. The typical chemical vibration of the powder and film samples was verified by Fourier transform infrared spectroscopy (FTIR) (Thermo scientific Nicolet 4700) in the wavenumber range from 4000 to 400 cm^{-1} using a KBr pellet. The reflectance of the powders and transmittance of the films were measured by UV-Vis-NIR spectroscopy (V570, Jasco Corp.) in the wavelength range of 220 to 2000 nm at the scan rate of 400 nm/min. The luminescent emitting spectra of the films and powders were measured by high-performance fluorescence spectroscopy (JASCO FP8500) connected to a Xenon lamp at the scan rate of 500 nm/min. The adhesion tests of the nanocomposite film were performed following the standard test methods of D 3359

– 97 (test method B) using transparent tape (Cellophane No. 252, 0.049 mm, adhesion strength of 3.1 N/10 mm, tensile strength of 36 N/10 mm, Sekisui Chemical Co., Ltd., Japan).

3. RESULTS AND DISCUSSION

3.1 Characterizations of the CMI, ZA, ZAG and CGx@ZAG Nanocomposites (Solutions and Powders)

The objective of this study was to obtain the LDH nanosheets treated in formamide for anchoring the Mo_6 cluster. The simple synthesizing process of ZA and ZAG was performed in air that leads to the formation of several kinds of LDH phases provided in Figure 1a. The major structure of the CO_3 type LDH phase (black circles) existing in ZA was confirmed by the XRD pattern which shows a series of peaks located at the 2θ-angles of 11.4, 23.4, 31.6, and 34.6° assigned to the (003), (006), (009), and (012) reflections, respectively.[46] The second series of peaks with a weak intensity assigned to the NO_3 type LDH phase locates at the 2θ-angle of 10, 20, and 30° for the (003), (006) and (009) reflections (green squares).[44] Besides, the remarkable patterns of the ZnO phase (pink lozenge) formed on the brucite-like sheets were also verified with the peaks at the 2θ-angles of 32°, 34°, and 36° in this study.[44, 46] The XRD pattern of ZA was used as a reference to provide evidence for identifying the ZAG structure from a similar synthesis

condition. It is reasonable to realize that the glycine-intercalated LDH (ZAG) results in a mixture of three crystalline structures. A minority phase of the NO_3 type LDH shows 2θ-angle peaks located with a slight shift to 9.7°, 19.1°, and 28.6° in comparison to that of the ZA pattern. Similarly, the second pattern assigned to the CO_3 typed LDH phase is shown with a significantly reduced intensity. Lastly, a new series characterized by the (003), (006), and (009) strong reflections corresponding to the 2θ angles of 7.2°, 13.9°, and 20.9° and d_{003} basal spacing value of about 1.22 nm is considered for the glycine type LDH (blue triangle). The FT-IR spectra shown in Figure S3 also provide evidence of the vibrational band assigned to the NO_3 and CO_3 groups in the ZA and ZAG powders that agree with the realized phase in the XRD results. Glycine is a good candidate to intercalate between LDH and limit the appearance of the CO_3 type LDH which is strongly generated in ZA. The pattern of the glycine-intercalated LDH (ZAG) obtained in this study agrees with the studies of the Zn-Al-Gly LDH material reported by Hibino.[46] Li and coworkers also claimed a similar pattern of the LDH intercalated glyphosate, which is almost the same size as glycine, simulating the horizontal or vertical geometries of the glycine molecules on the host layer.[47] The d_{003} value of about 1.22 nm means the total distance involving the 0.48 nm-sized metal host layer and 0.74 nm-sized interlayer space which adopts exchanged anions, adsorbed water, and vertical glycine monolayer or

bilayer. The glycine is reasonably anchored on the surface of the host layer by the hydrogen bonding with the hydroxyl group. In the case of the CG1@ZAG powder, the XRD pattern does not display the full series of crystalline peaks. As a result, the loading of the glycine/Mo_6 cluster mixture leads to destroying the big crystal of the ZAG as well as the nanosheets that have been formed from very efficient delamination. Moreover, as expected, the characteristic pattern of the CMI cluster compound completely disappears in the CG1@ZAG powder.

These results are supported by the HR-TEM images. Indeed, the CG1@ZAG powder only shows the crystalline part of LDH without the signal of the CMI cluster crystals (Fig. 1b). Even if it was not possible to observe single metal atoms dispersed in the LDH, the STEM-EDX mapping confirms the existence of Mo and I atoms assigned to the Mo_6 cluster (with a weak signal of the Cs^+ cations) and, additionally, N atoms assigned for glycine. The Cs^+ cations are mainly removed during the synthesis by the washing and centrifuge processes. Indeed, in the dispersing medium, the CMI cluster compound is mainly dissociated to form Cs^+ cations and $[Mo_6I^i_8I^a_6]^{2-}$ anions as depicted in Figure 1b which could explain the disappearance of the Cs^+ ion. Nevertheless, in solution, the I apical ligands could be quickly exchanged by a simple hydrolysis process to give new clusters with the theoretical formula $[Mo_6I^i_8I^a_{6-x-y}(OH)^a_x(H_2O)_y]^{y-2}$ $(x + y \leq 6)$, for instance,

the neutral compound $[Mo_6I^i_8(OH)^a_4(H_2O)^a_2]\ nH_2O$ (n = 2, 12, 14) (x = 4 and y = 2) revealed in the previous study.[48] More generally, the studies of the chlorine or bromine Mo_6 cluster compounds showed similar results.[49, 50] It is well known that the luminescent characteristic of the Mo_6 cluster compounds significantly depends on the nature of the ligand and counter cation or the different excitation-light sources.[51] This is particularly true for iodine-based compounds. Indeed, the CMI cluster compound shows a strong absorption below the 600-nm wavelength (Fig. 1c) and has no photoluminescent property (Fig. 1d) as already clarified,[51] whereas the $Cs_2Mo_6I^i_8X^a_6$ cluster family compounds with $X^a = CF_3COO$, C_2F_5COO, C_3F_7COO show the highest emission intensity.[34, 37, 52]

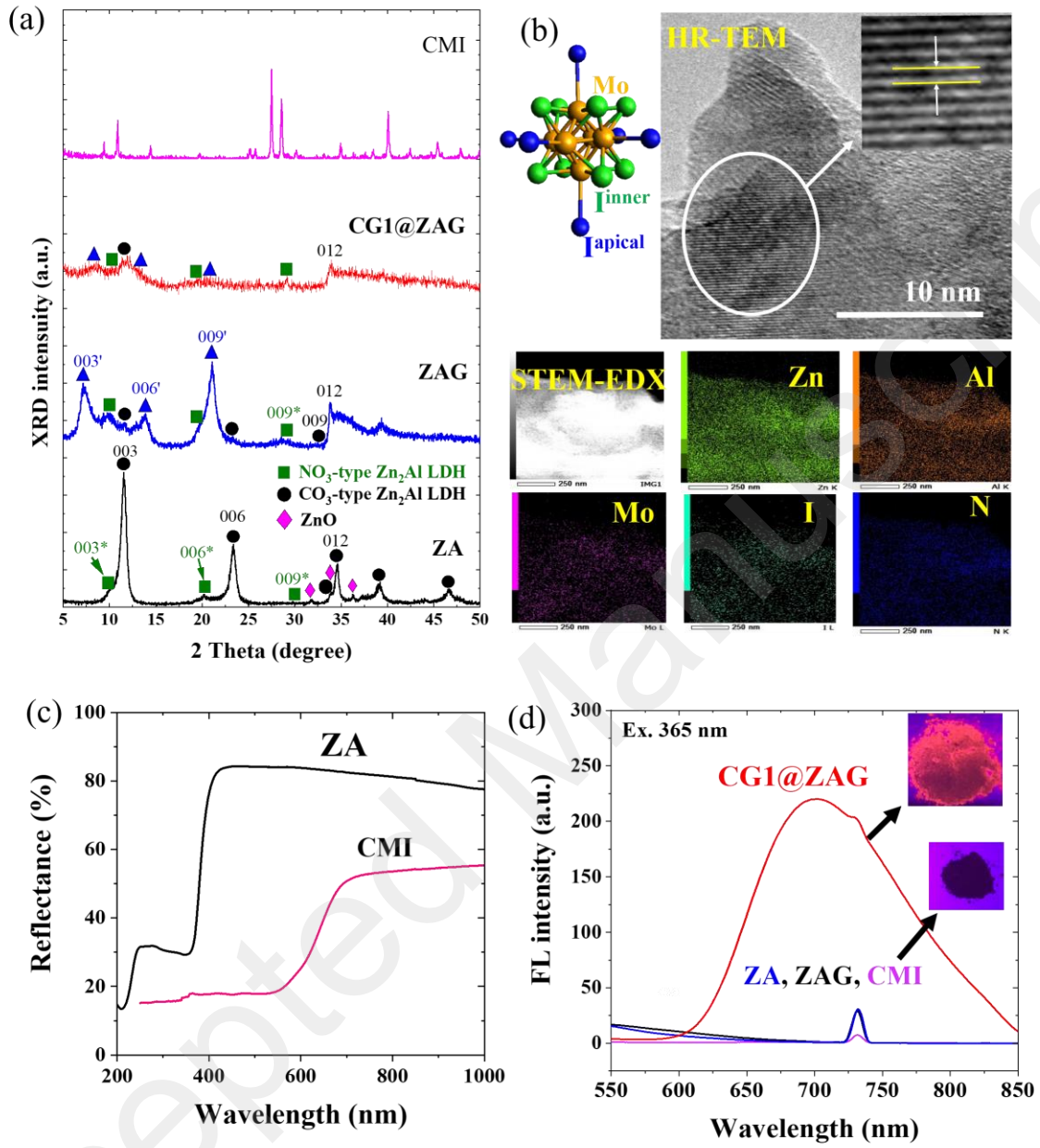

Figure 1. a) Powder XRD patterns of the Mo_6 cluster, ZA, ZAG and CG1@ZAG, b) the $[Mo_6I^i_8I^a_6]^{2-}$ cluster unit (Mo_6) schematic illustration, HR-TEM image and STEM-EDX mapping images of CG1@ZAG, c) the reflectance of the ZA and CMI powders, and d) FL spectra of CMI, ZAG, and CG1@ZAG powders with the small peak observed at 730

nm due to SHG.

To understand the optical properties of the CGx@ZAG nanocomposites, the influence of the glycine on the $[Mo_6I^i_8I^a_6]^{-2}$ cluster units dispersed in formamide was initially investigated. In a previous study, it was already demonstrated that the octahedral cluster complexes can be coordinated by the carboxylic acid groups of the glycine molecules.[53] For instance, the single crystals of the octahedral hexa-zirconium complexes coordinated with 4 anionic and 4 neutral glycines in aqueous solution have been growing by Pan et al., with the formula $[Zr_6(OH^-)_8(H_2O)_8(HGly)_4(Gly^-)_4]\cdot(SO_4^{2-})_6\cdot 14H_2O$.[54] To the best of our knowledge, there is no study reporting the interaction between the iodide hexa-molybdenum cluster compound and glycine but the results, presented below, suggest that they do exist. Unfortunately, a single crystal was not obtained, so we worked on solutions and powders. Indeed, the variation in the zeta potential and photoluminescence in solution were studied.

Table 1 shows the zeta potential parameters of different compounds and nanocomposites in formamide. The average zeta potential values are the result of three measurements at room temperature. The extremely negative value of the CG_0 solution indicates that the formula of the cluster units in solution could be $[Mo_6I^i_8I^a_{6-x}(OH)^a_x]^{-2}$ (x = 0 to 6 and y =

0) or $[Mo_6I^i_8I^a_{6-x-y}(OH)^a_x(H_2O)^a_y]^{-1}$ (x = 0 to 5 and y = 1), regarding the possible exchange of I apical ligands by H_2O or OH groups. They are present as impurities in the formamide solution. The negative zeta potential of the cluster in formamide is reduced with the addition of glycine that could indicate an interaction between the Mo_6 clusters and glycine. Generally, glycine simultaneously exists as a neutral $HOOC\text{-}CH_2\text{-}NH_2$ molecule and charged ($^{-}OOC\text{-}CH_2\text{-}NH_3^{+}$; $^{-}OOC\text{-}CH_2\text{-}NH_2$; $HOOC\text{-}CH_2\text{-}NH_3^{+}$) molecules depending on the dispersing medium and pH.[55] Based on the decrease in the negative zeta potential caused by the addition of the glycine, it is assumed that the positively charged glycine molecule possibly neutralizes the negatively charged surface of the iodide Mo_6 cluster unit through the ionic and/or covalent interactions as mentioned by Pan et al.[54] Additional studies to understand the structure of this new cluster are now in progress.

Regarding the CGx@ZAG nanocomposite suspension, the negatively charged cluster unit could be completely neutralized by the positive charge density on the LDH surface. On the other hand, the I apical ligands were exchanged by water molecules adsorbed in the interspace of LDH to form the neutral $[Mo_6I^i_8I^a_{6-x}(OH)^a_x(H_2O)^a_2]$ (x = 0 to 4) unit. As a result, the positive charges existing on the metal hydroxide surface determine the zeta potential of the CGx@ZAG suspension. This value gradually reduces with the increase in glycine concentration. In this study, the co-precipitated ZAG product shows a pH value

higher than 7 in formamide or MEK with the positive zeta potential values as seen in Table S2. The average zeta potential of the NO_3^- containing LDH is highly positive at a pH higher than 7 in an aqueous solution, also claimed by Kim et al.[56] In order to understand the existing state and interaction of the glycine and LDH, the FT-IR spectra were obtained for glycine, CMI, ZA, ZAG, and CG2@ZAG powders as illustrated in Figure S3. In the powder state, pure glycine almost shows strong absorption peaks at 1133, 1494, 1666 cm^{-1}, and a broad wavenumber range from 3200 to 2600 cm^{-1} assigned to the NH_3^+ group which specializes for the characteristic functional groups of the charged $^-OOC\text{-}CH_2\text{-}NH_3^+$ or $HOOC\text{-}CH_2\text{-}NH_3^+$ species.[57] However, these typical characteristic peaks of the NH_3 group completely disappear after glycine is combined with LDH in the ZAG phase that is agreeable with a previous study.[58] In parallel, proof for the existence of the $HOOC\text{-}CH_2\text{-}NH_2$ neutral molecules in ZAG is recognized by the stretching mode vibration assigned to the C=O group at 1760 cm^{-1} indicating the acid group that suggests an aggregated glycine phase separation. In the base medium containing LDH, glycine preferentially exists in the states of $^-OOC\text{-}CH_2\text{-}NH_2$ and $HOOC\text{-}CH_2\text{-}NH_2$. In the FT-IR spectrum of CG2@ZAG, besides the N-H bending mode vibration is assigned at 1625 cm^{-1}, the spectrum also shows a new signal at 1653 cm^{-1} that suggests the impact of hydrogen bonding on the NH_2 group. This is agreeable with the peak shifting in the

wavenumber range from 3000 to 3600 cm^{-1} to higher wavenumber. The absorption peak at 1590 cm^{-1} is indicated for the asymmetry stretching mode vibration of the COO group which insignificantly modifies in the nanocomposite. In summary, the NH_2 group of the $^{-}OOC\text{-}CH_2\text{-}NH_2$ anion is predicted to create the hydrogen bonding with the OH or H_2O apical ligands of the Mo_6 cluster and freely adsorbed H_2O molecules while the COO^{-} group will neutralize positive charges on the metal hydroxide surface of the LDH. The addition of the glycine in the base LDH medium will increase the charged $^{-}OOC\text{-}CH_2\text{-}NH_2$ anions which could generate ionic and/or covalent interactions with the positively charged LDH, resulting in the decreased positive zeta potential value.

Table 1. Average zeta potential values of the CMI cluster compound, glycine, CGx, and CGx@ZAG suspensions in formamide.

	Zeta potential (mV)	
CMI:Gly (wt%)	CGx	CGx@ZAG
1:0 (x=0)	-47.0±0.9	-
1:1 (x=1)	-29.0±1.2	27.5±0.8
1:5 (x=2)	-20.8±0.8	26.2±1.1
1:7.5 (x=3)	-16.0±1.0	22.5±1.2
1:10 (x=4)	-14.3±0.7	18.4±0.4
0:1	-18.2±0.5	-

Nevertheless, the presence of the Mo_6 cluster units in LDH is also demonstrated by the UV-Vis absorption (in formamide solution) and reflectance (with powder) measurements as shows in Figures S4a and 1c, respectively. Figure 1c illustrates a weak reflectance as well as a strong absorption below the 370-nm wavelength caused by LDH, while it is below the 600-nm wavelength observed for the CMI cluster compound. However, the optical adsorbing characteristic of the CG1@ZAG in formamide slightly shifts to a higher wavelength in comparison to that of the ZAG and CG1 compositions (Fig. S4a). In comparison to the ZA and ZAG powders, a strong red-shifted absorption of the CG1@ZAG nanocomposite due to the Mo_6 cluster compound is visible with a peak centered at 690 nm upon the $\lambda_{ex.}$ of 365 nm (Fig. 1d). For the solution, the most important modification is a shift in the maximum emission peaks for the different samples. It appears as an emission peak centered at 673 nm for the Mo_6 cluster-dissolved formamide, 663 nm for the CG1@ZAG-dissolved formamide, and 700 nm for the CG1-dissolved formamide upon the $\lambda_{ex.}$ of 400 nm (Fig. S4b). These shifts are significant and could be explained by the different interactions between glycine and LDH with the Mo_6 clusters. It is agreeable with a previous discussion about the reasonable change in the zeta potential. Indeed, the specific nature of the exchanged apical ligand is well known to affect the length of the Mo-Mo bonding that intervenes in the geometries.[33]

Regarding the optical properties, several points discussed above were confirmed: i) the ZA, ZAG, and CMI cluster powders do not show any luminescent-characterizing peak during light irradiation at 365 nm (Fig. 1d); ii) the Mo_6 cluster-dispersed formamide solution presents a strong red emission which is slightly modified by the addition of glycine during excitation at 400 nm (Fig. S4b); iii) the CGx@ZAG powder and solution exhibit a strong red emission upon excitation by UV light (Fig. S4b and 1d); iv) the nano-scaled CG1@ZAG sheets in formamide were proved though the Tyndall effect exhibits a strong photoluminescence characterized by a red-emitting light upon UV irradiation at 365 nm (Fig. S4b).

As already proposed, the Mo_6 clusters were possibly immobilized on graphene oxide nanosheets by covalent linking[59] or to a silica matrix by hydrogen bonds and/or by Mo-O-Si covalent linking[60] that modify the photoluminescent property of the cluster. In the previous work, the Mo-O-LDH chemical bonding was suggested between the $[Mo_6Cl^i_8Cl^a_{6-x-y}(H_2O)_x(OH)^a_y]^{x-2}$ (x = 0, 1 or 2 and y = 0, 1, 2, 3 ; x + y = 3) cluster and Zn-Al LDH that was revealed on the basic result of X-ray photoelectron spectroscopy.[61] In this study, one similarly suggested a hypothesis that the iodide Mo_6 cluster units would react with OH on the LDH surface to form Mo-O-LDH bonding and reduce the OH groups. Therefore, the interactions between the Mo_6 clusters and the metal-OH of LDH

is possible to stabilize the $[Mo_6I^i_8I^a_{6-x-y}(OH)^a_x\ (H_2O)_y]^{y-2}$ units on the surface of LDH. This leads to the modification of the molecular orbital diagram compared to that of the starting $[Mo_6I^i_8I^a_6]^{2-}$ unit, meanwhile inducing some change in the photoluminescence properties.[51, 52]

3.2. Characterization of the ZAG and CGx@ZAG Nanocomposite Films

Figure 2 shows the XRD patterns of the ZAG and CG_{1-4}@ZAG films prepared by EPD. It is realized that a series of peaks located at the 2θ angles of 7.21°, 13.44°, and 21.19° appear with the same peak position indicated in the pattern of the ZAG powder as seen in Figure 1a. The d_{003} value is about 1.22 nm which means a 1.2 nm-sized Mo_6 cluster unit is unable to occupy in the 0.74 nm-sized basal space between the host layers (0.48 nm).[45] In order to identify the compositions of the deposited film, the particle size distribution dissolved in the MEK/formamide medium as a suspension used for the EPD process was investigated and displayed in Figure S5. The ZAG suspension produced a uniform nanosheet size (0.54 μm) with a small size distribution (0.26 μm). When the mixture of the Mo_6 cluster and glycine (CG1-4) was introduced in the ZAG-dispersed MEK suspension, the coagulation occurred to form big particles with the size distribution in the range from 1 to 6 μm. Remarkably, CG3@ZAG shows a high volume of big particles with the obtained size of around 2 μm. Under an electric field, the small and uniform

nanosheets will preferentially move to the electrode with the same moment and the bigger particles will slowly arrive. The uniformity of the ZAG nanosheets of around 0.54 μm is an optimistic advantage to load a high intensity of the characteristic peak assigned to the glycine-LDH composition of ZAG as presented in Figure 1a. The treatment of formamide and glycine plays an extremely efficient role in the delamination of LDH. The CG1-3@ZAG films show insignificantly different patterns with a clearly lower intensity in comparison to that of ZAG. The existence of the CG during the delamination process produces the big coagulated LDH particles due to the hydrogen bondings and covalent-linkages between the added glycine and interspacing-adsorbed glycine or between the Mo_6 cluster and LDH as already suggested. When the higher concentration of glycine is added, the bigger the coagulated particles are obtained, resulting in a decrease of the delaminated LDH species with a small size (Fig. S5). As a result, the CG4@ZAG nanocomposite film contains a small amount of the delaminated glycine-LDH species and the majority of coagulated anion-typed LDH species. It is suggested that glycine existing in the original glycine-LDH species is removed by the strong interaction of a large amount of added glycine and formamide to reform the anion-typed LDH species then an agglomeration occurs. For this reason, the CG4@ZAG film shows a peak located at the 2θ angle of 11.5° which is assigned to the anion-typed LDH. It means that the

delamination of the ZAG in the formamide medium containing CG4 is not successful.

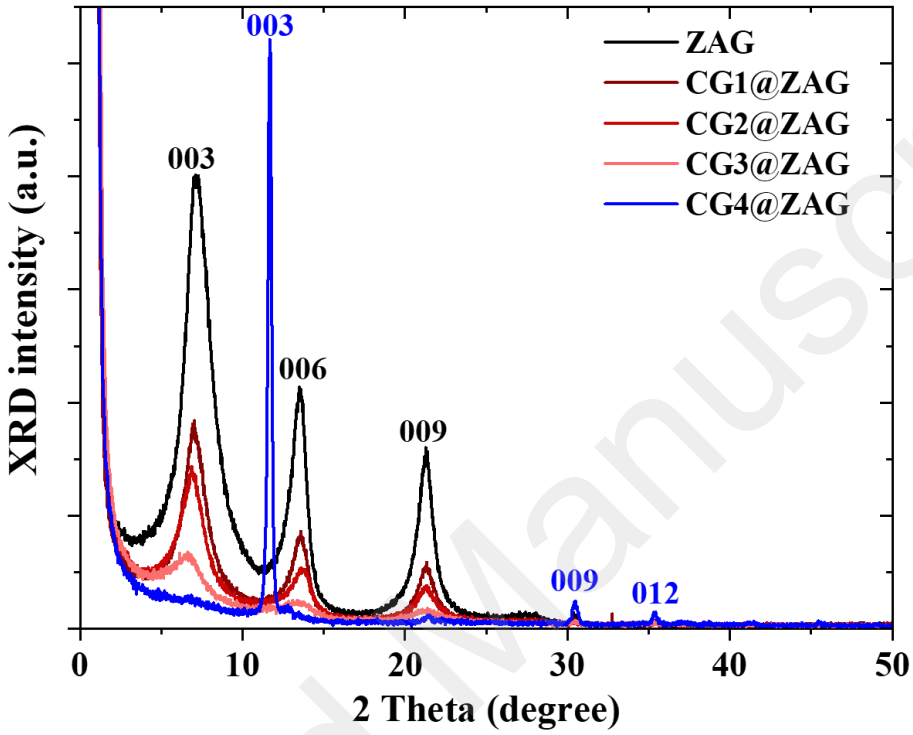

Figure 2. Thin-film XRD patterns of the ZAG, CG1-4@ZAG films prepared by the EPD.

The thin-film XRD pattern agrees with the lamellar structure observed in the cross-section FE-SEM images of the ZAG and CG1-2@ZAG films corresponding to the excellent transparency under visible light (Figs. 3a-c). A good condensing (see the cross-section) and homogeneous morphology of the ZAG film were obtained (Fig. 3a). Similarly, the CG1@ZAG and CG2@ZAG films also consist of a dense-layered structure and smooth

morphology (Fig. 3b and 3c). For the CG3@ZAG and CG4@ZAG samples, corresponding to the highest glycine concentrations, the transparency of the film decreased. This can be explained by the high number of defects observed in the layer as seen at the cross-section surface images, following the increase in the light scattering (Figs. 3d and 3e). It is understood that the interaction between glycine and formamide was extremely efficient to exfoliate the LDH nanosheets as provided in the ZAG film. However, not only the existence of the Mo_6 cluster but also the loaded glycine in the formamide medium leads to the formation of the nonhomogeneity of the particle size as seen in Figure S5. That indicates the reformation of the anion-typed LDH due to the removal of interspacing adsorbed glycine and then agglomeration occurs. Therefore, the optimal concentration of added glycine needs to be investigated. The glycine concentration in the CG3-4@ZAG films starts to show a random arrangement of the nanosheets intercalated with big particles creating a porosity on the surface and inside the layer. On the other hand, the high concentration of glycine could create a hydrophilic effect on Mo_6@ZAG and increase the miscibility between it and MEK that also limits the lamellar-structured reconstruction during the EPD. The red emission, at the exciting wavelength of 365 nm, was visually confirmed for all the CG1-4@ZAG films. This behavior indicates that EPD did not destroy the Mo_6 octahedron.

The HR-TEM and STEM images show the nano-scaled thin layer containing the agglomerated cluster units in the CG1@ZAG film prepared by the EPD (Figs. S6a, b, and c). The proof of the constituting elemental components of the nanocomposite was repeatedly provided by the STEM-EDX mapping. The energy spectrum completely confirms the existence of Zn, Al, Mo, I, and N atoms, followed by a weak sign of Cs atoms (Fig. S6d).

All these results are in agreement with the optical studies. As seen in Figures 3f and 3g, the optical properties are affected by the lamella structure of the nanocomposite films. As expected, the transmittance of the ZAG, CG1@ZAG and CG2@ZAG films is higher than 50% and agree with the transparency of the observed film photos taken by the camera under visible light (Fig. 3f). Additionally, the absorption characteristic of the hexanuclear iodide clusters indicated at wavelengths under 550 nm[52] is recognized as a fingerprint for the CGx@ZAG films while as it does not appear for the ZAG film. The absorption at the wavelengths over 1200 nm is assigned to the absorption of the indium tin oxide layer coated on glass. Figure 3g demonstrates, without a doubt, the red emission due to the Mo_6 atom clusters. In summary, the structure of the film should be composed of the $[Mo_6I^i_8I^a_{6-x-y}(OH)^a_x\ (H_2O)_y]^{y-2}$ cluster units and the nano-scaled ZAG layers, and the cluster is anchored on the LDH bound by the hydrogen bonding or covalent linkage.

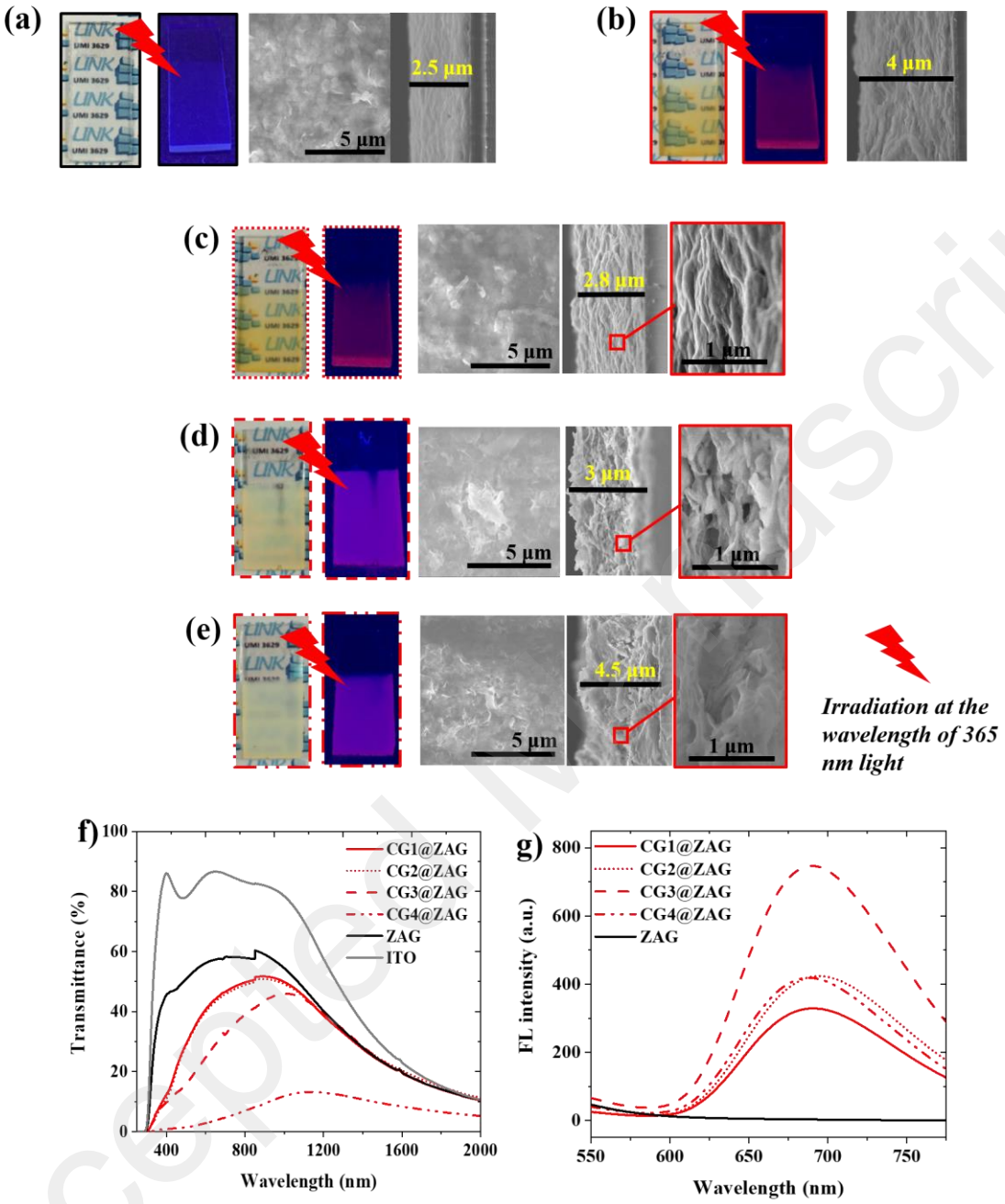

Figure 3. Photos of the UV-Vis irradiated films, the morphology (left) and cross-section (right) images by FE-SEM of the thin film prepared by EPD: a) ZAG, b) CG1@ZAG, c) CG2@ZAG, d) CG3@ZAG, e) CG4@ZAG. The transmittance (f) and fluorescence spectrum (g) of all the thin films.

At room temperature, the ZAG and CG2@ZAG films show a hydrophilic property with a contact angle less than 90 degrees, followed by insignificant damage on the surface after they are in contact with water (Fig. 4a and 4b). Both the ZAG and CG2@ZAG films were cut 1 mm apart and eleven cuts made to form the patterns on the surface as shown in Figures 4c and 4d for the adhesion measurement with tape. It can be seen that the film surface was slightly destroyed after testing the adhesion with tape. Based on the result of the 4B~5B classification of the ASTM D3359-97 standard test method, it can be concluded that the ZAG and CG2@ZAG films obtained an encouraging adhesion property as well as dense and strong interlayer interactions that positively affect the conductivity of the film.

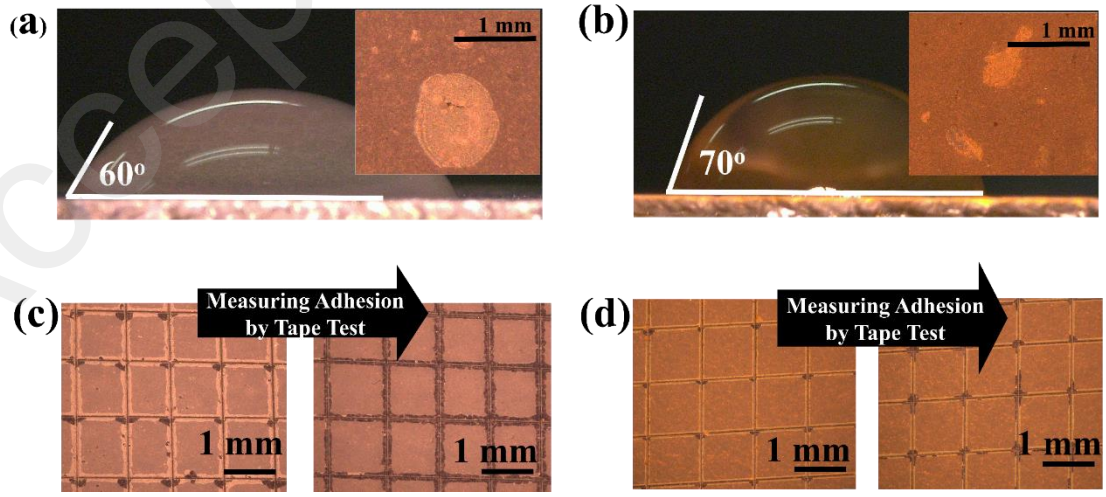

Figure 4. The 3D color morphology and water droplet photos for calculating the contact

angle of a) ZAG and b) CG2@ZAG. The morphology of the cut film with the patterns and after the adhesion measurement test of c) ZAG and d) CG2@ZAG.

3.3 Photocurrent Response of the ZAG and CG2@ZAG Nanocomposite Films

The EIS measurement illustrated in Figure S1 was applied for the optimally thick, dense, and homogeneous ZAG and CG2@ZAG films prepared by EPD at 25 V for 2 minutes. The quality and thickness of the films were controlled by the EPD parameters and the stability of the EPD suspension that is distributed by the amount of glycine, wet powder concentration, and the ratio between MEK and formamide. The thicknesses of the ZAG film and CG2@ZAG film are about 3.0 ± 0.2 μm and 3.4 ± 0.3 μm, respectively, prepared by the same EPD parameters. The light energy is transferred by an optical fiber through the ITO-coated glass to the deposited film. Based on Figure 3f, the absorption of the ITO-coated glass was about 60% at 320 nm, 30% at 370 nm, and 20% in the visible light range. As a result, the real intensity of the photon energy arriving at the surface of the material film corresponded to 40% at 320 nm, 70% at 370 nm, and 80% in the visible light range (400 nm – 600 nm). For this reason, we selected the excitation wavelengths with the peaks

centered at 320, 350, 370, 410, 440, 540, and 580 nm followed by the bandwidth of the light of about 10 nm. EIS of the films was measured in the humidity and temperature-controlled chamber.

Figure 5a shows the thin film photos and illustrates the sample-testing model for the DC and AC impedance (EIS) measurements with two ITO-coated glass electrodes connected to the source. The interlayer galleries of LDH contain hydroxyl ions, water, and exchanged anions for balancing the positively charged surface. The ionic conductivity is explained by the Grotthus mechanism and the hydroxyl ions will transport along with the adsorbed water molecules and hydroxyl groups of the host layer through covalent linking and hydrogen bonding.[62] The illustration scheme in Figure 5a suggests the possibly layered structure of the film and the transportation of the hydroxyl ions from the cathode to the anode when applying a bias. Besides the available absorbed hydroxyl anions on the host layer, they might be provided by the water hydrolysis reaction on the cathodic electrode during the EPD process.

Figure S7 shows the Nyquist plots of the ZAG film at the relative humidity (RH) of 50 %, ZAG film at the relative humidity (RH) of 80 %, and CG2@ZAG film at the relative humidity (RH) of 80 % measured by EIS at different temperatures. The Nyquist curve measured for the CG2@ZAG films at 303K and RH of 80% shows the compositions of

the solution resistance (R_s), charge transfer resistance (R_{ct}), and diffusional impedance or so-called Warburg Element (Z_w) (Fig. 5b). The Nyquist diagram was fitted by using a Randles equivalent circuit as depicted in Figure 5b. The R-value of the electrical conductivity in Eq.1 was calculated from the total resistance of the charge transfer resistance (R_{ct}) and the solution resistance (R_s) measured by Zview software. Generally, the semicircular arc becomes smaller corresponding to the decrease in the impedance versus the temperature increase. The decrease in the electrical resistance corresponds to the increase in the electrical conductivity as calculated by Eq. 1. The dependence of the electrical conductivity on the temperature of the films stored at RH 50% and RH 80% is illustrated in Figure 5c. The calculated electrical conductivities of ZAG at RH 50%, ZAG at RH 80%, and CG2@ZAG at RH 80% are 6.7×10^{-8}, 36.1×10^{-8}, and 4.1×10^{-8} S cm^{-1}, respectively. As already suggested, the Mo_6 cluster could react with the OH group on the LDH surface to form a covalent linkage and hydrogen bonding. These interactions cause a reduction of the free hydroxyl anion concentration in the film. Moreover, the water carrier was also kept by hydrogen bonding with the cluster and limits the anion diffusion in the film through the water carrier. These points lead to the result of the inferior ionic conductivity in the CG2@ZAG film (3.4 ± 0.3 μm) in comparison to the ZAG film (3.0 ± 0.2 μm). The electrical conductivity of the ZAG film increases with increased

relative humidity from 50% to 80%. In parallel, a linear rising tendency of the conductivity versus the temperature increase was observed. Simultaneously, the CG2@ZAG film stored at RH 80% displays a low electrical conductivity in comparison to the ZAG film under the same condition with a faster-increasing speed.

In general, the energy activation (E_a) was calculated from the relation with the electrical conductivity by the following equation:

$$\sigma T = A \cdot \exp(-E_a/RT) \qquad (2)$$

where A is a constant, T is the temperature, R is the gas constant, and E_a is the activation energy. The activation energy of the film was calculated from the slope of the fitted Arrhenius plots wherein the value of the natural logarithm of (σT) is linear versus the temperature (1/K). The activation energies of the ZAG (RH 50%), ZAG (RH 80%) and CG2@ZAG (RH 80%) films are 0.904 eV, 0.757 eV and 1.108 eV, respectively shown in Figure 5d. The E_a values agree with the Arrhenius equation (Eq. 2). This illustrates that a low E_a value corresponds to a higher electrical conductivity. With the reasonably calculated activation energy, the anionic conduction mechanism is suggested for all the films.[63] This result agrees with many previous studies for the LDH materials.[13-16] In summary, the existence of the Mo_6 cluster present on the metal hydroxide surface does not only not affect the anionic conduction mechanism of the LDH film but also shows a

similar tendency during the increasing temperature. Generally, the anionic conductivity is created by the transportation of the hydroxyl ions through water molecules as an important carrier by using the hydrogen bonding pathway. The Mo_6 cluster is suggested to create hydrogen bonding with the OH group and water adsorbed on the metal hydroxide surface and limits the diffusion of the hydroxyl anions, resulting in a reduction of the ionic conductivity. As a result, the conductivity of the Mo_6@LDH film is lower than that of the LDH film. This agrees with a higher E_a value for the Mo_6@LDH film. At a high temperature, the movement of the hydroxyl ions seems to be a priority in the cluster-modified space. This interesting point should be further investigated in the future.

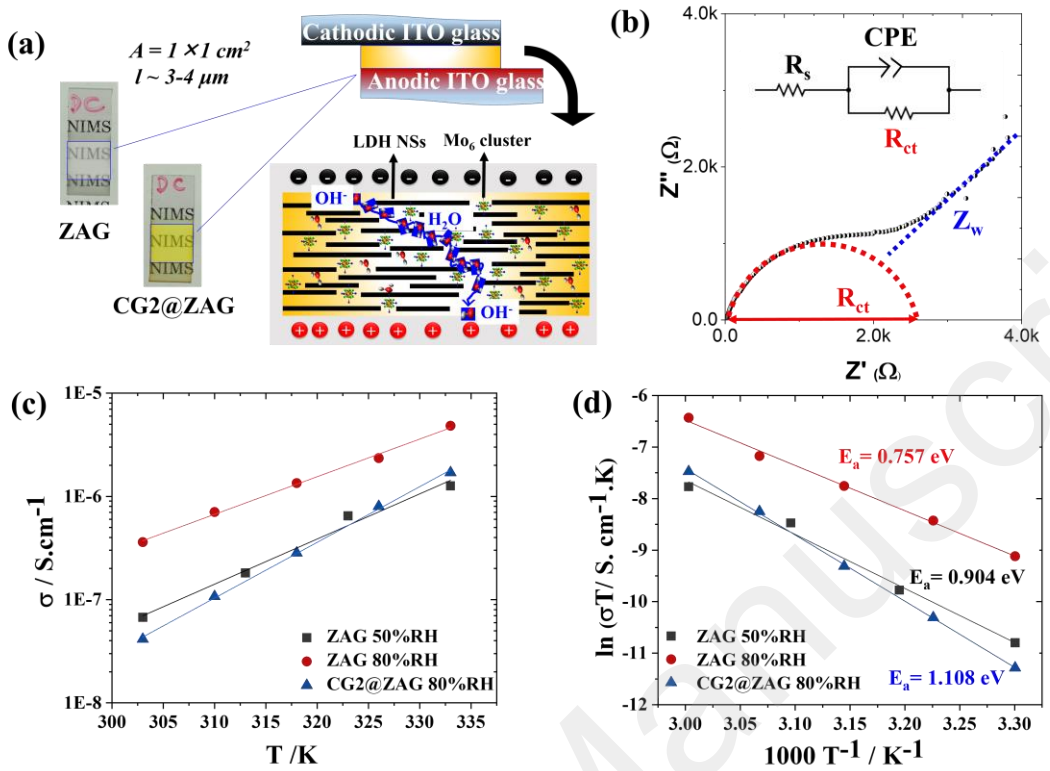

Figure 5. a) Photos of the ZAG and CG2@ZAG thin films under visible light and the transferring model of the proton through the film, b) Randles equivalent circuit for the electrochemical cell, Nyquist diagram and its fitting curve of CG2@ZAG at 303K and RH 80%, c) The dependence of the electrical conductivity vs. the temperatures, and d) Linear fits of the plots of ln (σT) versus T^{-1} of the ZAG and CG2@ZAG thin films at different temperatures and humidity.

The detailed investigation of the ionic conductivity versus the humidity is presented in Figure 6. Similarly, the reduction of the semicircular arc is observed that corresponds to the increase in the relative humidity from 25, 40, 60, 80, and 95% at 303 K (Fig. 6a and

b). The ZAG and CG2@ZAG films show a linear dependence of the ionic conductivity vs. the relative humidity (Figure 6c). The introduction of the Mo_6 cluster does not affect the proportionally increasing tendency of the ionic conductivity vs. the relative humidity. At high humidity, the increase of the water concentration adsorbed in the LDH forces an enhancement of ionic conductivity.

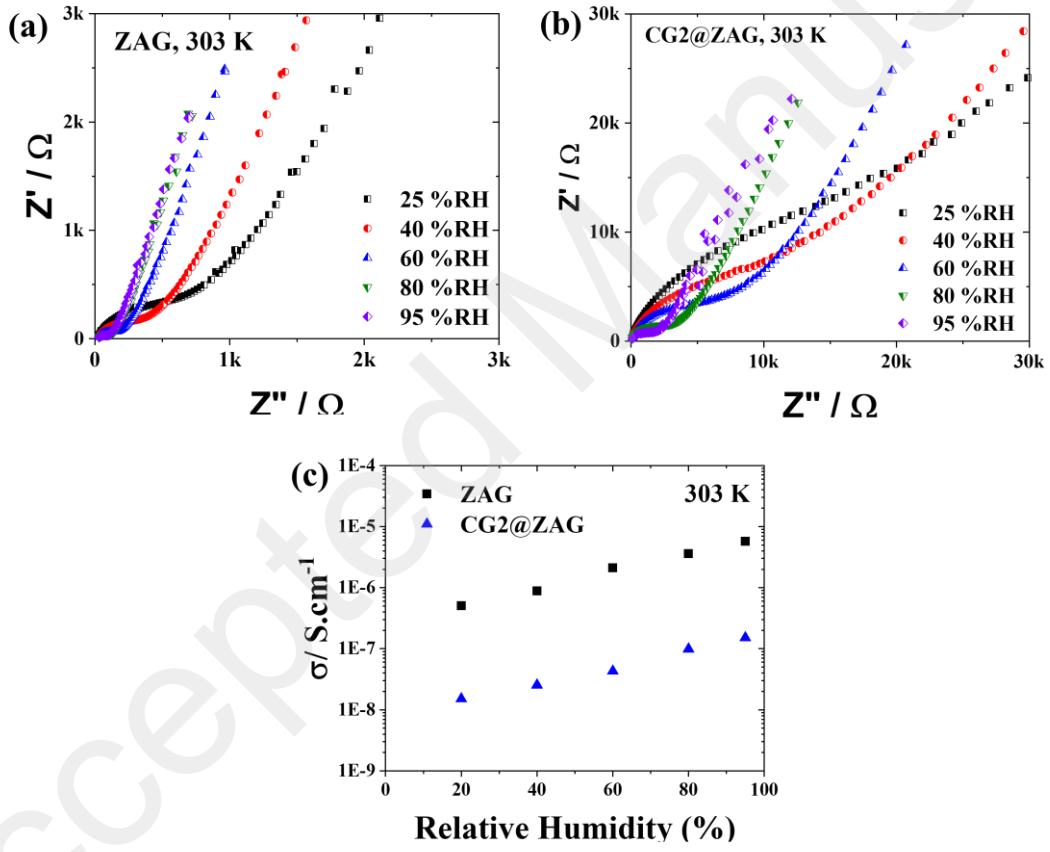

Figure 6. Nyquist plots for a) ZAG and b) CG2@ZAG at the temperature of 303 K with different relative humidities (RH %), and c) the dependence of the electrical conductivity vs. the relative humidity.

The photocurrent of the CG2@ZAG film was evaluated by DC measurements in the dark and under light illumination at various wavelengths. The applied bias was 1 V generated by a DC Keithley Model 2400 source. Figure 7a shows that the fluorescence peak in the wavelength range from 410 to 450 nm was caused by the metal hydroxide layers of the ZA and ZAG powders upon excitation at 370 nm. This result supports the photosensitization occurring in the LDH-based films upon excitation by UV light (Fig. 7b). The ZAG and CG2@ZAG films at the temperature of 303 K and RH of 50% and 80% result in the photocurrent response that proportionally fluctuates with the incident photon energy and reaches a higher intensity corresponding to the UV light range (Fig. 7b). However, the optical absorption of the ITO-coated glass at 320 nm obtains about 60% that limits the photon energy arriving at the material surface causing a reduction of the conductivity. For this reason, the photocurrent excited at 320 nm is observed to be more inferior than that excited at 350 nm. The small difference in the wavelength intensity does not affect the photocurrent result. The light adsorption and possible excitation during irradiation at specific wavelengths of the material mostly contribute to the photocurrent response. In the visible light range, the CG2@ZAG film displays a photosensitization possibility higher than that of the ZAG film due to the visible light absorption of the Mo_6 cluster.

Figure 7c illustrates a variation in the photocurrent responses under on –and -off switching of the continual UV-Vis light illumination at the fixed wavelengths centered at 320, 350, 370, 410, 440, 540 and 580 nm versus time. In the beginning, the films were applied a voltage for several minutes to gain a stable current value. At this stage, most of the hydroxyl ions are almostally transported from the cathode to anode under the electric field impact and a stable current is indicated for the electronic conductivity. Under illumination, the photocurrent responses are then characterized by a rapid enhancement during the first minutes before reaching saturation at 5 minutes. When the light was turned off, the current suddenly dropped to the original current value. Moreover, it can be seen in Figure 7c that the photocurrent intensity depends on the relative humidity following a directly proportional gradient. The fluctuating tendency of the photocurrent value is the same for the film controlled at the relative humidity of 50% and 80% at 303K. To confirm this tendency, an extra irradiation experiment for the ZAG film was performed at the excitation wavelengths from 580 nm to 320 nm versus time as seen in Figure S8, confirming a similar tendency of the photocurrent intensity in Figure 7c. Three interesting points are concluded in Figure 7c such as i) the ZAG film having a thinner thickness showed a photocurrent response higher than that of the CG2@ZAG upon irradiation below 440 nm, ii) the ZAG and CG2@ZAG films showing a linear dependence of the

photocurrent response vs. the humidity, and iii) only the CG2@ZAG film exhibited a photocurrent sensitization at $\lambda_{ex.}$ = 540 nm.

Reproducibility and stabilization of the photocurrent response is an important key for the photodetector application. For this reason, the repeatability of the photocurrent on the CG2@ZAG film with various thicknesses was performed at the $\lambda_{ex.}$ of 370 nm (Fig. 7d). The photocurrent from the on/off light switching operation always remains a constant value after the procedure is repeated several times. The basic electrical conductivity and the photocurrent response consistently depend on the film thickness. As illustrated here, the thicker film provides a higher current value and the fluctuation of the current is repeated with the same tendency.

As is known, the blank LDH could produce a photoconductive response with the light illumination from 350 nm to 420 nm.[28] In this study, the photosensitization of the blank LDH was extended in the visible light range of 440 nm as clearly observed in Figure 7c. However, only the CG2@ZAG film shows photosensitization in the visible light at the $\lambda_{ex.}$ of 540 nm as seen in Figure 7e. The optical absorbing characteristic of the cluster in the visible light range below 600 nm has produced the visible photosensitization for the CG2@ZAG film.

In general, the UV light irradiation could enhance the photocurrent of the LDH due to the

incident photon energy (hν) promoting the excitation of the electron (e_{CB}^-) from the valence band to a conducting band and leave a hole (h_{VB}^+) as seen in Eq. 1.[64] The electron created on the photoexcited LDH from Eq. 1 will enlarge the electronic flow on the metal hydroxide layer to increase the electrical conductivity. Besides, the hydroxyl radicals ($^{\cdot}OH$) generated from Eq. 2 are highly unstable due to their electron spin configuration is unpaired. The unpaired spin configuration forces the hydroxyl radical immediately capturing the free electron (e_{CB}^-) to form OH^- anion (Eq. 3) or missing electron from another hydroxyl radical ($^{\cdot}OH$) to form hydrogen peroxide (H_2O_2) (Eq. 4). The proton is also created from Eq. 2, however, the hydroxyl anion mobility is more dominant than the proton in LDH.[14] The immediate transport of the hydroxyl anions results in the enhancement of the total photocurrent. When the irradiation is off, the electron (e_{CB}^-) will immediately couple with the hole (h_{VB}^+) and the generation of the hydroxyl anions is simultaneously stopped, resulting in the disappearance of the photocurrent. As a result, the adsorbed water concentration at the different humidities will affect the generated hydroxyl concentration that causes an anionic conductivity when applying a bias. It could be suggested that the generated photoconductivity is produced by the electronic and anionic conductivities. The deep discussion about the role of the major conductivity mechanism during the irradiation should be performed in the future.

(Eq.1) $Zn/Al + h\nu \rightarrow (Zn/Al)(h_{VB}^{+}, e_{CB}^{-})$

(Eq.2) $(Zn/Al)\ h_{VB}^{+} + H_2O \rightarrow (Zn/Al) + {}^{\cdot}OH + H^{+}$

(Eq. 3) ${}^{\cdot}OH + e_{CB}^{-} \rightarrow OH^{-}$

(Eq. 4) ${}^{\cdot}OH + {}^{\cdot}OH \rightarrow H_2O_2$

This suggestion is also used to explain the linear dependence of the photoconductivity on the humidity for the CG2@ZAG film during light excitation at 540 nm. In this case, only the Mo_6 cluster plays an important role as an electron-supplying source during irradiation. When the Mo_6 cluster is excited by visible light (λ = 540 nm), the hole and electron pair are generated on the photoexcited cluster unit (Eq. 5). [59, 65] Similarly, the photocurrent value increases due to not only the electron generated from Eq. 5 but also the hydroxyl anion formed from Eq. 6 and Eq. 3. The photocurrent is therefore composed of electronic and anionic conductivities, which linearly depend on the humidity.

(Eq. 5) $(Mo_6\ cluster) + h\nu \rightarrow (Mo_6\ cluster)(h_{VB}^{+}, e_{CB}^{-})$

(Eq. 6) $(Mo_6\ cluster)(h_{VB}^{+}) + H_2O \rightarrow (Mo_6\ cluster) + {}^{\cdot}OH + H^{+}$

The smooth movement of the electron in the nanocomposite needs strong support from the homogeneously dense lamella structure, chemical bonding between the elemental

compositions, and homogeneous distribution of the Mo_6 cluster in the LDH matrix. For this result, the unique chemical interaction existing between the metal oxide layer and the cluster plays an important role in the transportation of the electron through the interspace.

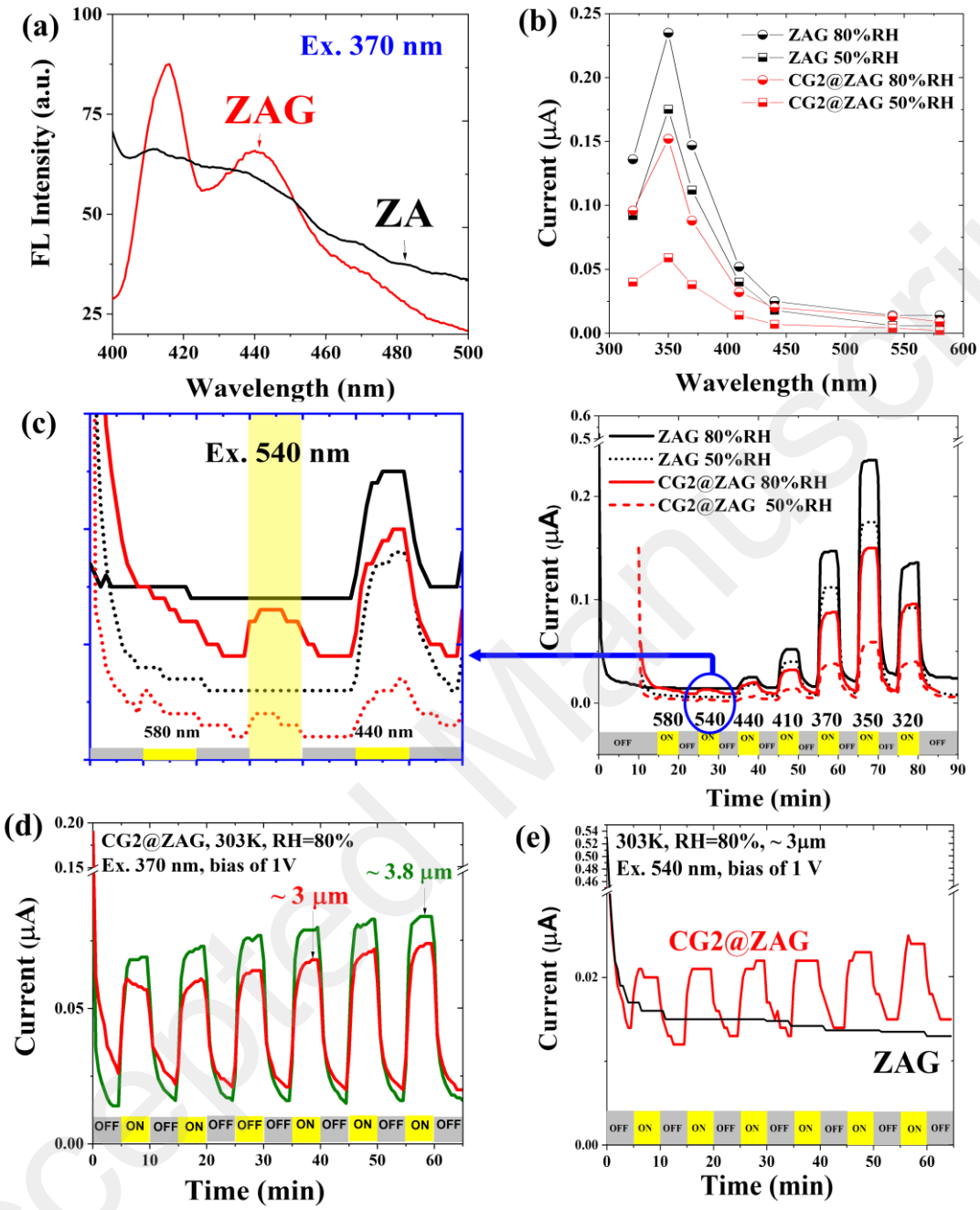

Figure 7. a) The fluorescence spectra of the ZA and ZAG powder under excitation of 370 nm, b) The dependence of the photocurrent intensity versus the exciting wavelength, c) The photocurrent controlled by on-off switching procedure under the illumination by

different light wavelengths of the ZAG and CG2@ZAG films measured at RH of 50% and RH of 80 % and 303 K versus the time. d) The repeatability of the photocurrent responses repeated versus the time of the CG2@ZAG films at $\lambda_{ex.}$ = 540 nm for different thicknesses. e) The repeatability of the photocurrent responses of the ZAG and CG2@ZAG films versus the on-off switching time with $\lambda_{ex.}$ = 540 nm.

Figure 8a shows the electrical property versus the temperature of the ZAG and CG2@ZAG films measured by EIS. These results were calculated from the impedance semicircular arc presented in Figure S9. The impedance of the films controlled at 80% RH was measured in the dark and at $\lambda_{ex.}$ of 370 or 440 nm. Both the ZAG and CG2@ZAG films present a small increase in the conductivity during irradiation with a slightly preferential value for the excitation wavelength of 370 nm. The results are in agreement with the increasing tendency of the photocurrent intensity measured by DC (Figure 7b). The activation energies (E_a) of the ZAG and CG2@ZAG films at different irradiation conditions calculated from the Arrhenius plots in Figure 8b result in 0.75± 0.01 eV and 1.12 ± 0.01 eV, respectively. The E_a of the CG2@ZAG films is higher than that of the ZAG film in all cases. As mentioned in the previous discussion, the Mo_6 cluster reduces the diffusion of the hydroxyl anion resulting in a decrease of the conductivity and increase

in the activation energy. The E_a value of the CG2@ZAG and ZAG films presents an insignificant modification with and without irradiation.

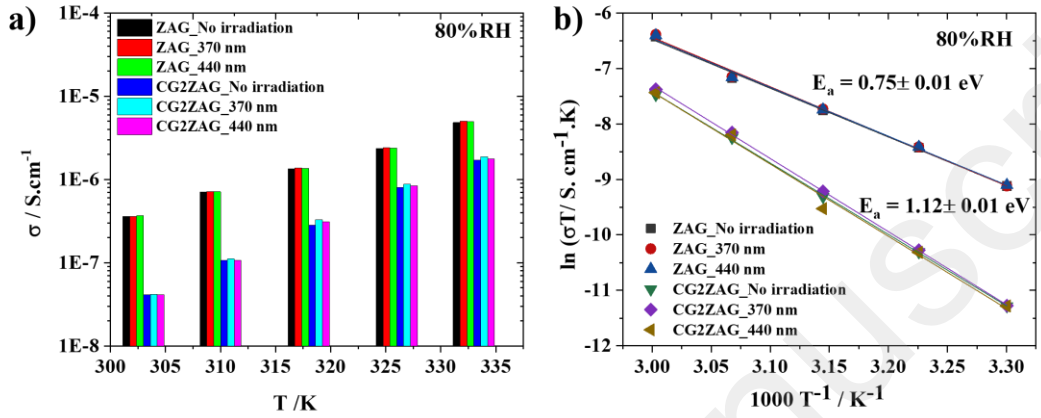

Figure 8. a) The dependence of the electrical conductivity on the temperature and b) Linear fits of the plots of ln (σT) versus T^{-1} of the ZAG and CG2@ZAG films stored at RH 80% in the dark and at $\lambda_{ex.}$ = 370, 440 nm.

In summary, for the first time, the photochemical behavior of the molybdenum halide cluster was combined with the electrical property of LDH aiming to create a material exhibiting a photocurrent response upon visible light irradiation. Its photo-electrical property stabilization is valid for the development of an optical sensing device. Many reasonable hypothesizes have discussed the origin of the redox, photophysical, and photochemical properties of the Mo_6 cluster based on the molecular structure, chemical compositions, and their intrinsic interactions.[33,37,38,51] Moreover, the proton-conducting properties of the $(H)_2[Mo_6X_8(OH)_6]\bullet 12H_2O$ (X = Cl, Br) have been clarified through the

hydrogen-bond network that develops between apical hydroxyl groups and the adsorbed water molecules.[66] Kuttipillai et al. also suggested that the counter cations can play an important role in charge injection, transport, recombination, and exciton formation in the electrically pumped devices fabricated from the core cluster.[67] The interaction between the neighboring clusters and electrical pumped host material is an important key to impact the tunneling, recombination dynamics, and exciton formation. These ideas could be used to explain in this study that the covalent bonding, ionic interaction, or hydrogen bonding possibly occurring between the OH or H_2O groups induced the Mo_6 clusters and metal hydroxide layers to play a role as the closed bridges for the unique electron transportation. A uniquely closed network is the essential parameter to assure the continually occurring electrical transportation that results in a high photo-electrical sensitization, stabilization, reproducibility, and utilizing for a device-developing strategy.

4. CONCLUSION

For the first time, thin and transparent Mo_6 cluster-functionalized LDH films, CGx@ZAG (x=1-4), were successfully prepared by EPD. The morphology, the dense lamellar structure, and the elemental composition of the films were fully characterized by utilizing SEM/HR-TEM/EDX analyses, and XRD measurements. The optical properties and photocurrent responses were fully measured. The CG1-2@ZAG films display a strong

UV-Vis absorption under 550 nm and red emission light at the wavelength of 690 nm when excited by the UV-Vis lights. The obtained conductivity value of the CG2@ZAG was about 4.1 10^{-8} S. cm^{-1} at RH 80% and 303K with the activation energies (E_a) about 1.108 eV indicating an ionic conduction mechanism. The CG2@ZAG film conductivity can be controlled by the relative humidity and temperature. Remarkably, the films present very good photocurrent responses, measured by both DC and AC impedance measurements, during excitation in the UV light range, and visible light from 410 to 540 nm due to the visible light adsorbing Mo_6 clusters. The reproducibility and stabilization of the sample's photocurrent response were established. The excellent properties obtained from the CGx@ZAG films prepared by the EPD process make them be considered as promising candidates for photo-humidity sensing and a photodetector.

ASSOCIATED CONTENT

Supporting Information. Schematic fabrication and conductive-testing system of the films; FTIR and UV-Vis absorption spectra of the nanocomposite solutions and powders; the particle size distribution of the nanocomposite powders; FE-SEM and EDX mapping images of the nanocomposite film; Nyquist plots of the nanocomposite films.

AUTHOR INFORMATION

Corresponding Author

Tetsuo UCHIKOSHI: Group Leader, Optical Materials Field, Fine Particles Engineering Group, Research Center for Functional Materials, National Institute for Materials Science (NIMS), 1-2-1 Sengen, Tsukuba, Ibaraki 305-0047, Japan. Email: UCHIKOSHI.Tetsuo@nims.go.jp,

Thi Kim Ngan NGUYEN: NIMS Special Researcher, Optical Materials Field, Fine Particles Engineering Group, Research Center for Functional Materials, National Institute for Materials Science (NIMS), 1-2-1 Sengen, Tsukuba, Ibaraki 305-0047, Japan. Email: NGUYEN.Thikimngan@nims.go.jp.

Author Contributions

The manuscript was written through the contributions of all the authors. All the authors have approved the final version of the manuscript.

ACKNOWLEDGMENT

These studies were carried out as a part of the France-Japan International Collaboration Framework (UMI3629 LINK). The authors wish to thank Mr. D. Lechevalier and Dr. M. Zhou of Saint-Gobain KK (Tokyo, Japan) for their significant support involved in LINK

and related activities.

Notes

The authors declare no competing financial interest.

REFERENCES

1. Gant, P. ; Huang, P.; Pérez de Lara, D.; Guo, D.; Frisenda A. R. Castellanos-Gomez, A Strain Tunable Single-Layer MoS_2 Photodetector, Mater. Today, 2019, 27, 8-13.

2. Boruah, B. D. Zinc Oxide Ultraviolet Photodetectors: Rapid Progress from Conventional To Self-Powered Photodetectors, Nanoscale Adv., 2019, 1, 2059-2085.

3. Premkumar, S.; Nataraj, D.; Bharathi, G.; Ramya, S.; Thangadurai, T. D. Highly Responsive Ultraviolet Sensor Based on ZnS Quantum Dot Solid with Enhanced Photocurrent, Sci. Rep., 2019, 9, 18704-18718.

4. Shen, Y.; Jones, A. H.; Yuan, Y.; Zheng, J.; Peng, Y.; Mil, B. V.; Olver, K.; Sampath, A. V.; Parker, C.; Opila, E.; Campbell, J. C. Near Ultraviolet Enhanced 4H-SiC Schottky Diode, Appl. Phys. Lett., 2019, 115, 261101-261105.

5. Shkir, M.; T.Khan, M.; Ashraf, I. M.; Almohammedi, A.; Dieguez, E.; AlFaify, S. High-performance Visible-Light Photodetectors Based on Inorganic CZT and InCZT Single Crystals, Sci. Rep., 2019, 9, 12436-12445.

6. Shao, D.; Zhu, W.; Xin, G.; Liu, X.; Wang, T.; Shi, S.; Lian, J.; Sawyer, S. A High-Performance Uv–Visible Dual-Band Photodetector based on An Inorganic Cs_2SnI_6 Perovskite/ZnO Heterojunction Structure, J. Mater. Chem. C, 2020, 8, 1819-1825.

7. Mohapatra, L.; Parida, K. A Review on The Recent Progress, Challenges, and Perspective Of Layered Double Hydroxides As Promising Photocatalysts, J. Mater. Chem. A, 2016, 4, 10744-10766.

8. Zubair, M.; Daud, M.; McKay, G.; Shehzad, F.; Al-Harthi, M. A. Recent Progress In Layered Double Hydroxides (LDH)-containing Hybrids As Adsorbents for Water Remediation, Appl. Clay Sci., 2017, 143, 279-292.

9. Mishra, G.; Dash, B.; Pandey, S. Layered double hydroxides: A Brief Review From Fundamentals to Application As Evolving Biomaterials, Appl. Clay Sci., 2018, 153, 172-186.

10. Chuva, N.; Gilmour, R.; Gedar, V.; Micusik, M.; Omastova, M.; Heister, K.; Man, P.; Fraissard, J.; Zaitsev, V. Layered Double Hydroxides As The Next Generation Inorganic Anion Exchangers: Synthetic Methods Versus Applicability, Adv. Colloid Interface Sci., 2017, 245, 62-80.

11. Xie, Y.; Yuan, X.; Wua, Z.; Zeng, G.; Jiang, L.; Peng, X.; Li, H. Adsorption Behavior and Mechanism of Mg/Fe Layered Double Hydroxide with Fe_3O_4-carbon Spheres on The

Removal of Pb(II) and Cu(II), J. Colloid Interface Sci., 2019, 536, 440-455.

12. Abo El-Reesh, G. Y.; Farghali, A. A.; Taha, M.; Mahmoud, R. K. Novel Synthesis of Ni/Fe Layered Double Hydroxides Using Urea and Glycerol And Their Enhanced Adsorption Behavior For Cr(VI) Removal, Sci. Rep., 2020, 10, 587-603.

13. Pizzoferratoa, R.; Ciottaa, E.; Ferraria, I.V.; Bragliaa, M.; Medaglia, P.G.; Mattoccia, A.; Di Giamberardino, L.; Richetta, M.; Knauth, P.; Di Vona, M.L. Ionic Conductivity of Zn-Al Layered Double Hydroxide Films Grown on Aluminum Substrate, Solid State Ionics, 2018, 314, 30-35.

14. Sun, P.; Ma, R.; Bai, X.; Wang, K.; Zhu, H.; Sasaki, T. Single-layer Nanosheets with Exceptionally High and Anisotropic Hydroxyl Ion Conductivity, Sci. Adv. 2017, 3, 1602629-1602637.

15. Zhang, P.; Yamaguchi, T.; Nair, B. N.; Miyajimaa, K.; Anilkumar, G. M. Mg–Al Layered Double Hydroxides: A Correlation Between Synthesis-Structure and Ionic Conductivity, RSC Adv., 2014, 4, 41051-41058.

16. Pizzoferrato, R.; Ciotta, E.; Ferrari, I. V.; Narducci, R.; Pasquini, L.; Varone, A.; Richetta, M.; Antonaroli, S.; Braglia, M.; Knauth, P.; Di-Vona, M.L. Layered Double Hydroxides Containing an Ionic Liquid: Ionic Conductivity and Use in Composite Anion Exchange Membranes, Chem. Electro. Chem, 2018, 5, 2781-2788.

17. Li, X.Z.; Liu, R.S.; Guo, Y. Polyaniline-intercalated Layered Double Hydroxides: Synthesis and Properties for Humidity Sensing, RSC Adv., 2016, 6, 63099-63106.

18. Polese, D.; Mattoccia, A.; Giorgi, F.; Pazzini, L.; Ferrone, A.; Di Giamberardino, L.; Maiolo, L.; Pecora, A.; Convertino, A.; Fortunato, G.; Medaglia, P. G. Layered Double Hydroxides Intercalated with Chlorine Used As Low Temperature Gas Sensors, Procedia Eng., 2015, 120, 1175-1178.

19. He, Y.; Wang, R.; Jiao, T.; Yan, X.; Wang, M.; Zhang, L.; Bai, Z.; Zhang, Q.; Peng, Q. Facile Preparation of Self-Assembled Layered Double Hydroxide- Based Composite Dye Films As New Chemical Gas Sensors, ACS Sustainable Chem. Eng. 2019, 7, 10888-10899.

20. Shi, W.; He, S.; Wei, M.; Evans, D. G.; Duan, X. Optical pH Sensor with Rapid Response Based on a Fluorescein-Intercalated Layered Double Hydroxide, Adv. Funct. Mater. 2010, 20, 3856-3863.

21. Wang, F.; Wang, T.; Sun, S.; Xu, Y.; Yu, R.; Li, H. One-step Synthesis Of Nickle Iron Layered Double Hydroxide/Reduced Graphene Oxide/Carbon Nanofibers Composite As Electrode Materials for Asymmetric Supercapacitor, Sci. Rep., 2018, 8, 8908-8918.

22. Li, R.; Hu, Z.; Shao, X.; Cheng, P.; Li, S.; Yu, W.; Lin, W.; Yuan, D. Large Scale Synthesis of NiCo Layered Double Hydroxides for Superior Asymmetric Electrochemical

Capacitor, Sci. Rep., 2016, 6, 18737-18746.

23. Tyagi, A.; Joshi, M. C.; Agarwal, K.; Balasubramaniama, B.; Gupta, R.K. Three-dimensional Nickel Vanadium Layered Double Hydroxide Nanostructures Grown On Carbon Cloth For High-Performance Flexible Supercapacitor Applications, Nanoscale Adv., 2019, 1, 2400-2407.

24. Prestopino, G.; Arrabito, G.; Generosi, A.; Mattoccia, A.; Paci, B.; Perez, G.; Verona-Rinati, G.; Medaglia, P. G. Emerging Switchable Ultraviolet Photoluminescence in Dehydrated Zn/Al Layered Double Hydroxide Nanoplatelets, Sci. Rep., 2019, 9, 11498-11510.

25. Li, Z.; Wan, S.; Shi, W.; Wei, M.; Yin, M.; Yang, W.; Evans, D. G.; Duan, X. A Light-Triggered Switch Based on Spiropyran/Layered Double Hydroxide Ultrathin Films, J. Phys. Chem. C, 2015, 119, 7428-7435.

26. Cho, S.; Kwag, J.; Jeong, S.; Baek, Y.; Kim, S. Highly Fluorescent and Stable Quantum Dot-Polymer-Layered Double Hydroxide Composites, Chem. Mater., 2013, 25, 1071−1077.

27. Zhang, M.; Han, D.; Lu, C.; Ming Lin, J.M. Organo-Modified Layered Double Hydroxides Switch-On Chemiluminescence, J. Phys. Chem. C, 2012, 116, 6371-6375.

28. Jeon, C.W.; Lee, S.S.; Park, I.K. Flexible Visible-Blind Ultraviolet Photodetectors

Based on ZnAl- Layered Double Hydroxide Nanosheet Scroll, ACS Appl. Mater. Interfaces, 2019, 11, 35138−35145.

29. Wang, X.; Ning, X.; Shao, Q.; Ge, S.; Fei, Z.; Lei, J.; Hou, B. ZnFeAl-Layered Double Hydroxides/TiO_2 Composites As Photoanodes For Photocathodic Protection Of 304 Stainless Steel, Sci. Rep., 2018, 8, 4116-4124.

30. Ding, P.; Luo, F.; Wang, P.; Xia, W.; Xu, X.; Hu, J.; Zeng, H. Photo-induced Charge Kinetic Acceleration In Ultrathin Layered Double Hydroxide Nanosheets Boosts The Oxygen Evolution Reaction, J. Mater. Chem. A, 2020, 8, 1105-1112.

31. Cotton, F. A. Metal Atom Clusters in Oxide Systems, Inorg. Chem., 1964, 3, 1217-1220.

32. Jackson, J.A.; Turro, C.; Newsham, M.D.; Nocera, D.G. Oxygen Quenching of Electronically Excited Hexanuclear Molybdenum and Tungsten Halide Clusters, J. Phys. Chem., 1990, 94, 4500-4507.

33. Costuas, K.; Bulou, A. A.; Fontaine, B.; Cuny, J.; Gautier, R.; Mortier, M.; Molard, Y.; Duvail, J. L.; Faulques, E.; Cordier, S. Combined Theoretical And Time-Resolved Photoluminescence Investigations of $[Mo_6Br^i_8Br^a_6]$ Metal Cluster Units: Evidence of Dual Emission, Phys. Chem. Chem. Phys., 2015, 17, 28574-28585.

34. Dechezelles, J.F.; Aubert, T.; Grasset, F.; Cordier, S.; Barthou, C.; Schwob, C.; Maître,

A.; Vallée, A. R.A.L.; Cramail, H.; Ravaine, S. Fine Tuning Of Emission Through The Engineering of Colloidal Crystals, Phys. Chem. Chem. Phys., 2010, 12, 11993-11999.

35. Efremova, O. A.; Brylev, K. A.; Vorotnikov, Y. A.; Vejsadova, L.; Shestopalov, M. A.; Chimonides, G. F.; Mikes, P.; Topham, P. D.; Kim, S. J.; Kitamurah, N.; Sutherland, A. J. Photoluminescent Materials Based on PMMA and A Highly-Emissive Octahedral Molybdenum Metal Cluster Complex, J. Mater. Chem. C, 2016, 4, 497-503.

36. Kirakci, K.; Kubát, P.; Dusˇek, M.; Fejfarová, K.; Sícha, V.; Mosinger, J.; Lang, K. A Highly Luminescent Hexanuclear Molybdenum Cluster–APromising Candidate toward Photoactive Materials, Eur. J. Inorg. Chem., 2012, 19, 3107-3111.

37. Kirakci, K.; Kubát, P.; Langmaier, J.; Polívka, T.; Fuciman, M.; Fejfarovád, K.; Lang, K. A.A Comparative Study Of The Redox and Excited State Properties of $(nBu_4N)_2[Mo_6X_{14}]$ and $(nBu_4N)_2[Mo_6X_8(CF_3COO)_6]$ (X = Cl, Br, or I), Dalton Trans., 2013, 42, 7224-7232.

38. Vorotnikova, N. A.; Vorotnikov, Y. A.; Novozhilov, I. N.; Syrokvashin, M. M.; Nadolinny, V. A.; Kuratieva, N. V.; Benoit, D. M.; Mironov, Y. V.; Walton, R. I.; Clarkson, G. J.; Kitamura, N.; Sutherland, A. J.; Shestopalov, M. A.; A.Efremova, O. ^{23}Electron Octahedral Molybdenum Cluster Complex $[\{Mo_6I_8\}Cl_6]^{-}$, Inorg. Chem., 2018, 57, 811-820.

39. Ivanova, M.N.; Vorotnikov, Y.A.; Plotnikova, E.E.; Marchuk, M. V.; Ivanov, A.A.; Asanov, I.P.; Tsygankova, A.R.; Grayfer, E.D.; Fedorov, V.E.; Shestopalov, M.A. Hexamolybdenum Clusters Supported on Exfoliated h-BN Nanosheets for Photocatalytic Water Purification, Inorg. Chem., 2020, 59, 6439-6448.

40. Neaime, C.; Amela-Cortes, M.; Grasset, F.; Molard, Y.; Cordier, S.; Dierre, B.; Mortier, M.; Takei, T.; Takahashi, K.; Haneda, H.; Verelstf, M.; Lechevallier, S. Time-gated Luminescence Bioimaging with New Luminescent Nanocolloids Based on $[Mo_6I_8(C_2F_5COO)_6]^{2-}$ Metal Atom Clusters, Phys. Chem. Chem. Phys., 2016, 18, 30166-30173.

41. Renaud, A.; Nguyen, T.K.N.; Grasset, F.; Raissi, M.; Guillon, V.; Delabrouille, F.; Dumait, N.; Jouan, P.Y.; Cario, L.; Jobic, S.; Pellegrin, Y.; Odobel, F.; Cordier, S.; Uchikoshi, T. Preparation by Electrophoretic Deposition Of Molybdenum Iodide Cluster-Based Functional Nanostructured Photoelectrodes For Solar Cells, Electrochi. Acta, 317, 2019, 737-745.

42. Nguyen, T. K. N.; Renaud, A.; Dierre, B.; Bouteille, B.; Wilmet, M.; Dubernet, M.; Ohashi, N.; Grasset, F.; Uchikoshi, T. Extended Study on Electrophoretic Deposition Process of Inorganic Octahedral Metal Clusters: Advanced Multifunctional Transparent Nanocomposite Thin Films, Bull. Chem. Soc. Jpn., 2018, 91, 1763-1774.

43. Kirakci, K.; Cordier, S.; Perrin, C. Synthesis and Characterization of $Cs_2Mo_6X_{14}$ (X = Br or I) Hexamolybdenum Cluster Halides: Efficient Mo_6 Cluster Precursors For Solution Chemistry Syntheses, Z. Anorg. Allg. Chem., 2005, 63, 411-416.

44. Ahmed, A.A.A.; Tali, Z.A.; Hussein, M.Z.; Zakaria, A. Zn–Al Layered Double Hydroxide Prepared At Different Molar Ratios: Preparation, Characterization, Optical And Dielectric Properties, J. Solid State Chem., 2012, 191, 271-278.

45. Hibino, T. Delamination of Layered Double Hydroxides Containing Amino Acids, Chem. Mater., 2004, 16, 5482-5488.

46. Starukh, G. Photocatalytically Enhanced Cationic Dye Removeal with Zn-Al Layered Double Hydroxides, Nanoccale Reseach Letters, 2017, 12, 391-399.

47. Li, F.; Zhang, L.; Evans, D. G.; Forano, C.; Duan, X. Structure and Thermal Evolution of Mg–Al Layered Double Hydroxide Containing Interlayer Organic Glyphosate Anions, Thermochimica Acta, 2004, 424, 15–23.

48. Mikhaylov, M.A.; Abramov, P.A.; Komarova, V.Y.; Sokolov, M.N. Cluster aqua/hydroxocomplexes Supporting Extended Hydrogen Bonding Networks. Preparation and Structure of A Unique Series of Cluster Hydrates $[Mo_6I_8(OH)_4(H_2O)_2]\cdot nH_2O$ (n = 2, 12, 14), Polyhedron, 2016, 122, 241-246.

49. Zarate, X.; Schott, E.; Soto, L.A.; Tagle, R. R. A Family of Octahedral Molybdenum

Cluster Complexes $[Mo_6Cl_8(H_2O)_n(OH)_{6-n}]^{n-2}$ with n = 0-6 as a pH-sensors: A Theoretical Study, Chem. Phys. Lett., 2013, 567, 39-42.

50. Nguyen, T.K.N.; Dierre, B.; Grasset, F.; Renaud, A.; Cordier, S.; Lemoine, P.; Ohashi, N.; Uchikoshi, T. Formation Mechanism of Transparent Mo_6 Metal Atom Cluster Film Prepared by Electrophoretic Deposition, J. Electrochem. Soc. 2017, 164, 412-418.

51. Dierre, B.; Costuas, K.; Dumait, N.; Paofai, S.; Amela-Cortes, M.; Molard, Y.; Grasset, F.; Cho, Y.; Takahashi, K.; Ohashi, N.; Uchikoshi, T.; Cordier, S. Mo_6 Cluster-Based Compounds for Energy Conversion Applications: Comparative Study of Photoluminescence And Cathodoluminescence, Sci. Technol. Adv. Mater., 2017, 18, 458-466.

52. Sokolov, M. N. ; Mihailov, M. A. ; Peresypkin, E. V. ; Brylev, K. A. ; Kitamura, N. ; Fedin. V.P. Highly Luminescent Complexes $[Mo_6X_8(n\text{-}C_3F_7COO)_6]^{2-}$ (X = Br, I), Dalton Trans., 2011, 40, 6375–6377.

53. Xiang, S.; Hu, S.; Sheng, T.; Fu, R.; Wu, X.; Zhang, X. A Fan-Shaped Polynuclear Gd_6Cu_{12} Amino Acid Cluster: A "Hollow" and Ferromagnetic $[Gd_6(\mu3\text{-}OH)_8]$ Octahedral Core Encapsulated by Six $[Cu_2]$ Glycinato Blade Fragments, J. Am. Chem. Soc., 2007, 129, 15144-15146.

54. Pan, L.; Heddy, R.; Li, J.; Zheng, C.; Huang, X. Y.; Tang, X.; Kilpatrick, L. Synthesis

and Structural Determination of a Hexanuclear Zirconium Glycine Compound Formed in Aqueous Solution, Inorg. Chem., 2008, 47, 5537-5539.

55. Hernández, B.; Pflüger, F.; G.Kruglik, S.; Ghomi, M. Protonation–Deprotonation of The Glycine Backbone As Followed By Raman Scattering and Multiconformational. Analysis, Chem. Phys., 2013, 425, 104-113.

56. Kim, T. H.; Hong, I. T.; Oh, J. M. Size and Surface Charge-Controlled Layered Double Hydroxides for Efficient Algal Flocculation, Environ. Sci.: Nano, 2018, 5, 183-190

57. Rosado, M. T.; Duarte, M. L. T.S.; Fausto, R. Vibrational Spectra of Acid and Alkaline Glycine Salts, Vibrational Spectroscopy, 1998, 16, 35–54.

58. Wang, N.; Huang, Z.; Li, X.; Li, J.; Ji, S.; An, Q. F. Tuning Molecular Sieving Channels of Layered Double Hydroxides Membrane with Direct Intercalation of Amino Acids, J. Mater. Chem. A, 2018, 6, 17148–17155.

59. Kumar, P.; Mungse, H. P.; Cordier, S.; Boukherroub, R.; Khatri, O.P.; Jain, S.L. Hexamolybdenum clusters supported on graphene oxide: Visible-light Induced Photocatalytic Reduction of Carbon Dioxide Into Methanol, Carbon, 2015, 94, 91-100.

60. Aubert, T.; Hurtado, F. C.; Esnault, M. A.; Neaime, C.; Chauvel, D. L.; Jeanne, S.; Pellen, P.; Roiland, C.; Polles, L. L.; Saito, N.; Kimoto, K.; Haneda, H.; Ohashi, N.; Grasset, F.; Cordier, S. Extended Investigations on Luminescent $Cs_2[Mo_6Br_{14}]$@SiO_2

Nanoparticles: Physico-Structural Characterizations and Toxicity Studies, J. Phys. Chem. C., 2013, 117, 20154-20163

61. Nguyen, T.K.N.; Matsui,Y.; Shirahata,N.; Dumait, N.; Cordier, S.; Grasset, F.; Ohashi, N.; Uchikoshi, T. Zn-Al layered double hydroxide-based nanocomposite functionalized with an octahedral molybdenum cluster exhibiting prominent photoactive and oxidation properties. Appl. Clay Sci., 2020, 196, 105765.

62. Agmon, N. The Grotthuss mechanism, Chem. Phys. Let., 1995, 244, 456-462.

63. Kreuer, K. D.; Rabenau, A.; Weppner, W. Vehicle Mechanism, A New Model for The Interpretation of The Conductivity of Fast Proton Conductors, Angew. Chem. Int. Ed. Engl., 1982, 21, 208-209.

64. Mohapatra, L.; Patra D.; Parida, K.; Zaidi, S. J. Enhanced Photocatalytic Activity of a Molybdate-Intercalated Iron-Based Layered Double Hydroxide. Eur. J. Inorg. Chem. 2017, 3, 723–733

65. Barras, A.; Das, M. R.; Reddy, R.; Devarapalli,; Shelke, M. V.; Cordier, S.; Szuneritsa, S.; Boukherrou, R. One-pot Synthesis of Gold Nanoparticle/Molybdenum cluster/Graphene Oxide Nanocomposite and Its Photocatalytic Activity, Appl. Catal. B, 2013, 130-131, 270-276.

66. Daigre, G.; Cuny, J.; Lemoine, P.; Amela-Cortes, M.; Paofai, S.; Audebrand, N.; Le

Gal La Salle, A.; Quarez, E.; Joubert, O.; Naumov, N. G.; Cordier, S. Metal Atom Clusters as Building Blocks for Multifunctional Proton Conducting Materials: Theoretical and Experimental Characterization, Inorg. Chem., 2018, 57, 9814-9825.

67. Kuttipillai, P. S.; Zhao, Y.; Traverse, C. J.; Staples, R. J.; Levine, B. G.; Lunt, R. R. P hosphorescent Nanocluster Light-Emitting Diodes, Adv. Mater. 2016, 28, 320-326.

For Table of Contents Only